Multi-level Random Sample Consensus Method for Improving Structured Light Vision Systems

Zhankun Luo[1], Yaan Zhang[2], Lizhe Tan[1]
[1]Department of Electrical and Computer Engineering, Purdue University Northwest, Indiana, USA
[2]Department of Electrical and Computer Engineering, University of Missouri, Missouri, USA
Email: luo333@pnw.edu;yznbm@missouri.edu;lizhetan@pnw.edu

***Abstract*—The paper proposes a structured light vision system equipped with multi-cameras and multi-laser emitters for object height measurement or 3D reconstruction. The proposed method offers a better accuracy performance over a single camera system. To tackle the intersections produced by laser emitters in the projected image plane, we propose a multi-level random sample consensus (MLRANSAC) algorithm to separate the intersection points instead of using the traditional methods such as time division and color division techniques. Our experiments demonstrate that the MLRANSAC algorithm can perform effectively.**

***Keywords*—Structured light vision; Multi-camera; RANSAC.**

I. Introduction

Nowadays, structured light systems are widely utilized in computer vision for 3D reconstruction procedures [1]-[3]. Since the line structured light vision system offers high precision and anti-interference capability, it has also been selected as an effective measurement method in many industrial applications, including robotics, machine inspection, autopilot, architecture, archaeology, agriculture [4]-[9] and Mars exploration [10]-[12]. Furthermore, laser emitters [13]-[16] consisting of beam laser lines and projectors [17]-[19] with encoded patterns are frequently used as light sources to employ their geometric characteristics.

Conventionally, a vision system with a beam source and a camera installed at various angles gives sufficient information for an essential 3D reconstruction [20]. A typical technique favors parallel lines [4] rather than crossings in the projected patterns to evade image processing difficulties. For instance, a laser-scanned scheme applies one single laser line at a time. It later reconstructs the shape by transferring the object along with a specific orientation [13] or turning the system along with a fixed point [3], [7]. For projector systems, the gray-code pattern [15], [17], is broadly employed with the time-domain encode method. The projector system assigns a gray-code sequence for each pixel's position by repeatedly posting patterns with white and black bands. Then it applies the square dots as a post pattern in the projector system [18].

Nevertheless, in the circumstances where the crossing emitting lines are applied, the conventional method may not conduct well the 3D-reconstruction owing to the vagueness of labeling points around the crossing points [21]-[24]. In this study, we tackle the crossing line pattern in a structured light system using multiple laser emitters and numerous cameras similar to [25]. We derive a framework for the structured light vision system with multiple cameras and multiple laser emitters. Then we propose a multi-level RANSAC (MLRANSAC) algorithm to classify the unlabeled laser projected points into different sets effectively. Eventually, we validate the proposed methods. The paper's significant contributions are: (1) deriving a framework for multiple laser emitters and multiple cameras; and (2) applying multi-level RANSAC algorithm to separate intersection points. Finally, we adopt additional multiple cameras to improve the measurement accuracy over the recently developed system [26].

II. Structured Light Vision System with Multiple Laser Emitters and Multiple Cameras

Fig. 1 displays our measurement scheme. It consists of N laser emitters with red, green, and other options, a processing platform and M high-resolution cameras. As presented in Fig. 1, the camera coordinate and world coordinate and are denoted by $o_{ck}x_{ck}y_{ck}z_{ck}$ $k=1,2,\ldots,M$ and $oxyz$. Notice that the equation: $z=0$ gives the horizontal level in the world coordinate. We assume that the triangular plane's projection on the plane of $z=0$ exists and can be taken by cameras.

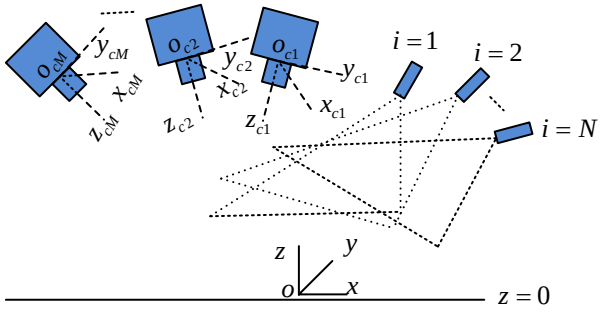

Fig. 1. Height measurement system.

A. Measurement Methods

In our study, we employ the camera pinhole model. We can formulate a perspective projection for camera k as below:

$$X_{ck} = z_{ck} A_k^{-1} \bar{I}_{pk} \tag{1}$$

$$\bar{X}_{ck} = \begin{bmatrix} R_k & t_k \\ 0 & 1 \end{bmatrix} \bar{X} \tag{2}$$

For conciseness of illustration, we define

$X = (x \quad y \quad z)^T$ - the point in the world coordinate;

$X = (x \quad y \quad z \quad 1)^T$ - the variant form of X;

$X_{ck} = (x_{ck} \quad y_{ck} \quad z_{ck})^T$ - the point in the kth camera coordinate;

$\bar{X}_{ck} = (x_{ck} \quad y_{ck} \quad z_{ck} \quad 1)^T$ - the variant form of X_{ck};

$I_{pk} = (u_k \quad v_k)^T$ - the point in the image pixel coordinate from the kth camera; and

$\bar{I}_{pk} = (u_k \quad v_k \quad 1)^T$: the variant form of I_{pk}.

Here is the intrinsic matrix A_k, in the form of below:

$$A_k = \begin{bmatrix} \alpha_k & c_k & u_{0k} \\ 0 & \beta_k & v_{0k} \\ 0 & 0 & 1 \end{bmatrix} \tag{3}$$

where for camera *k*: α_k and β_k are the scaling factors between camera coordinates and pixel coordinates in x and y axes. Moreover, u_{0k} and v_{0k} are the image coordinates corresponding to the optical axis. The c_k is the skewness in for two image axes. This $[R_k \quad t_k] = [r_{1k} \quad r_{2k} \quad r_{3k} \quad t_k]$ denotes the rotation and translation connecting the camera coordinates and the world coordinates.

For each characteristic j-th point on the i-th laser plane, namely formed by the i-th laser emitter, it can be expressed as

$$\bar{X}_{cLk}(i,j) = (x_{cLk}(i,j) \quad y_{cLk}(i,j) \quad z_{cLk}(i,j) \quad 1)^T$$

and the i-th laser plane is designated by

$$\pi_i = (a_i \quad b_i \quad c_i \quad -1)^T .$$

We can derive the following equation based on basic formulas:

$$X_{cLk}(i,j) / z_{ck}(i,j) = A_k^{-1} \bar{I}_{pk}(i,j) \tag{4}$$

$$\pi_i \bar{X}_{cLk}(i,j) = 0, \quad j = 1,2,\cdots,J \tag{5}$$

For the given projected point $\bar{I}_{pk}(i,j)$ and equation (4), we can achieve

$$X_{cLk}(i,j) / z_{cLk}(i,j) = [x_{cLk}(i,j) / z_{cLk}(i,j) \quad y_{cLk}(i,j) / z_{cLk}(i,j) \quad 1] \tag{6}$$

With the calibrated triangular plane i, and (5), we can eventually produce

$$z_{cLk}(i,j) = 1/(a_i x_{cLk}(i,j) / z_{cLk}(i,) + b_i y_{cLk}(i,j) / z_{cLk}(i,j) + c_i) \tag{7}$$

From (1), $X_{ck}(i,j) = X_{cLk}(i,j)$ can be achieved. Finally, we obtain

$$\bar{X}(i,j) = \begin{bmatrix} R_k & t_k \\ 0 & 1 \end{bmatrix}^{-1} \bar{X}_{ck}(i,j) \tag{8}$$

With the calibrated intrinsic and extrinsic parameters and all the laser planes, we can apply our developed multi-level RANSAC (MLRANSAC) algorithm to perform the 3D reconstruction.

B. Calibration

We model the camera after Zhang's method [23], where the pixel coordinates and the world coordinates are represented by $\tilde{m} = (u \quad v \quad 1)^T$ $M = (x \quad y \quad z \quad 1)^T$. Using a pinhole camera model, there is a connection between pixel coordinates and the world coordinates.

$$s\tilde{m} = A_k \, [R_k \; t_k] \, M = A_k \, [r_{1k} \; r_{2k} \; r_{3k} \; t_k] \, M \tag{9}$$

Assuming $z = 0$ (floor plane) in the model, (9) becomes

$$s\tilde{m} = A_k \, [r_{1k} \; r_{2k} \; t_k] \, \tilde{M} \tag{10}$$

where s is the depth to the camera pinhole and $\tilde{M} = (x \quad y \quad 1)^T$. The effective methodology for solving an intrinsic matrix A and extrinsic parameters (10) can be found in [23].

Each triangular plane $\pi_i = (a_i \quad b_i \quad c_i \quad -1)$ required in (5) $i = 1,2,\cdots,N$ is calibrated independently. As shown in Fig. 1, set the floor plane $z = 0$ in the world coordinate to be $(0 \quad 0 \quad 1 \quad 0)^T$. We can derive the floor plane to the camera coordinate as

$$\pi_{0k} = \begin{bmatrix} R_k & t_k \\ 0 & 1 \end{bmatrix}^{-T} \begin{bmatrix} 0 \\ 0 \\ 1 \\ 0 \end{bmatrix} = [A_k \quad B_k \quad C_k \quad D_k]^T \tag{11}$$

The projected j-th image points $X_{ck}(i,j)$ must be on the plane of the checkerboard in the camera coordinates during calibration, namely,

$$\pi_{0k}^T X_{ck}(i,j) = 0 \text{ for } j = 1,2,\cdots,J \tag{12}$$

In other words, we can write it as such a form

$$z_{ck}(i,j)[A_k x_{ck}(i,j) / z_{ck}(i,j) + B_k y_c(i,j) / z_{ck}(i,j) + C_k] = -D_k \quad \text{for } j = 1,2,\cdots,J \tag{13}$$

Notice that $x_{ck}(i,j) / z_{ck}(i,j)$ and $y_{ck}(i,j) / z_{ck}(i,j)$ in (13) can be calculated via the projected pixel points, namely,

$$X_{ck}(i,j) / z_{ck}(i,j) = A_k^{-1} \bar{I}_{pk}(i,j)) \text{ for } j = 1,2,\cdots,J \tag{14}$$

Then we can obtain $z_{ck}(i,j)$ in the camera coordinate with (13). Eventually, we can compute characteristic points in the following way.

$$X_{cLk}(i,j) = X_{ck}(i,j) = z_{ck}(i,j) A_k^{-1} \bar{I}_p(i,j) \tag{15}$$

Thus the characteristic points are known for each triangular laser plane $\pi_{ik} = (a_{ik} \quad b_{ik} \quad c_{ik} \quad -1)$, namely,

$$\pi_{ik} \bar{X}_{cLk}(i,j) = 0, \quad j = 1,2,\cdots,J \tag{16}$$

and with M trials for different checkerboard orientations on the floor plane at $z = 0$, we have:

$$\pi_{ik}\bar{X}_{cLk}(i,j)_m = 0.,\ j = 1,2,\cdots,J,\ m = 1,2,\cdots,M \quad (17)$$

Finally, we apply the least-squares method to solve the i-th triangular plane, namely, $\pi_i = (a_i \quad b_i \quad c_i \quad -1)$.

III. Multi-level Random Sample Consensus Algorithm

For the scenario where multiple cameras and laser emitters are used, one of the difficult tasks is to classify the intersection points in the image projection to their corresponding triangular planes. The time-division and color division can be used. Still, time-division processing is slow since it operates for each laser emitter one at a time while the color division requires the emitters with different light color sources, usually red, green, and blue light sources. Besides, the color division is sensitive to the illuminance environment during the measurement. The multi-level RANSAC (MLRANSAC) algorithm is an effective alternative [26].

During the operation stage, the projected points from the i-th laser emitter on the checkerboard at z=0 are extracted. The least-squares method can be utilized to find its linear model, $\omega_i = (\lambda_1(i) \quad \lambda_2(i) \quad \lambda_0(i))^T$ subject to the plane equation $\omega_i(u(j) \quad v(j) \quad 1)^T = 0$. For the stage at level 1, we choose K points randomly from the elicited point set. The normal vector is used to initialize the slope of the linear fitting model. We calculate K linear trial equations as the following equation:

$$\bar{\lambda}_0(k) = -(\lambda_1(i)u_k + \lambda_2(i)v_k),\ k = 1,2,\cdots,K \quad (18)$$

Then we determine the number of points within the maximum allowable distance d. The selected line equation is the equation composes of the maximum number of points, namely,

$$\omega_i = (\lambda_1(i) \quad \lambda_2(i) \quad \lambda_0(i))^T,\ i = 1,2,\cdots,N \quad (19)$$

Fig. 2 depicts the scenario for the case of $N = 2$.

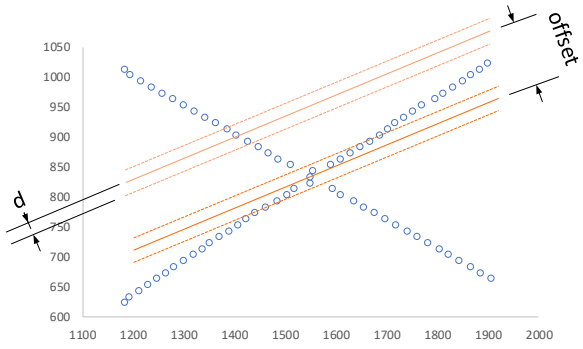

Fig. 2. The first level of MLRANSAC algorithm.

Besides, we begin to treat (19) as the "best straight line," drawing the intersection of the i-th laser emitter. 2 sample points are randomly selected from the K point set to recalculate a new straight line. Using all the received straight lines to show the following test on all the extracted points. In the case of that the distance from a test point to the straight line is less than d, then we consider, the test point is on the laser plane and add it to the point set corresponding to the laser plane. The total number of points in the laser set related to the line could be greater than that of the "best straight line." Moreover, the angle between the initial one and the straight line in (19) within a specific threshold. Then the "best straight line" is updated by the current straight line. After iteration for K times, the final line equation is obtained. Repeating the same process for N laser planes, we obtain the final N projected equations and N sets of the projected points. Figs. 2-4 show the case of $N = 2$.

Eventually, there could still be some points that cannot be decided on a specific laser plane they are on (see Fig. 5). The distance factor and direction factor are introduced at level 3. The distance factor is a distance ratio (d_1 / d_2) for the undecided point. d_1 is a distance from the undecided point to the specific laser intersection (for example, red), while d_2 is the distance between the undecided point and the other laser intersection (for example, green). In the case of that the distance factor is greater than a certain threshold, then we classify the undecided point to this specific laser point set. Fig. 6 describes the case of $N = 2$.

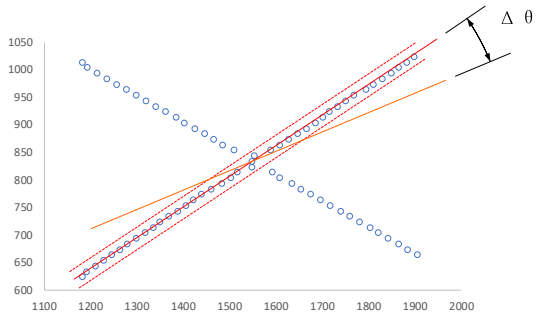

Fig. 3. The second level of MLRANSAC algorithm.

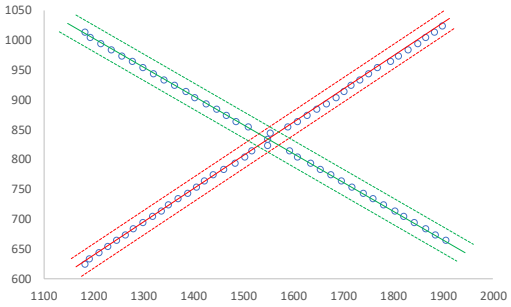

Fig. 4. The "best straight line."

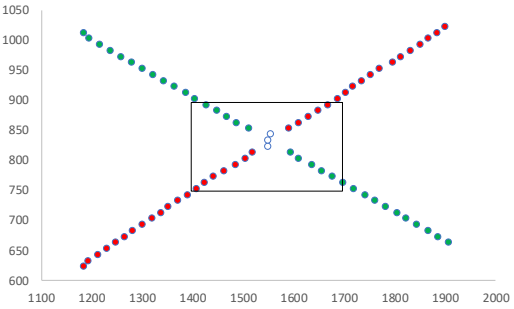

Fig. 5. Some points that cannot be decided to which laser emitters.

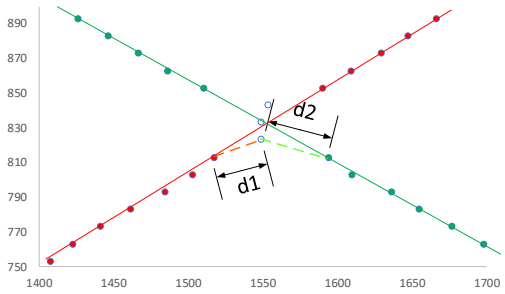

Fig. 6. The distance factor.

The direction factor is defined as the cosine angle value $\cos(\Delta\theta)$ between two directions as shown in Fig. 7, in which the angle is formed from the line segment of the undecided point and the nearest point in the specific laser set and the specific laser projected line. The undecided point is classified as the one laser point set if the direction factor is closer to one among the other laser point sets, as shown in Fig. 7 the case of $N = 2$.

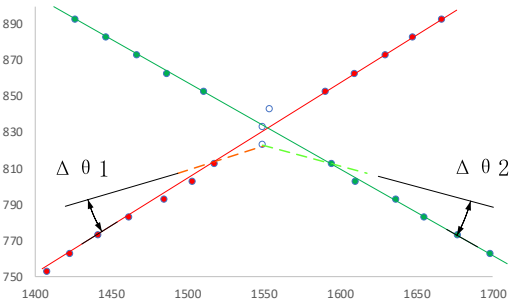

Fig. 7. The direction factor.

IV. Experiments and Processing

The designed measurement system includes, red and green laser emitters [27], 9 * 10 square checkerboard, a processing platform and two high-resolution cameras (Basler acA2500-14gc GigE camera with ON Semiconductor MT9P031 CMOS sensor, 14 frames per second, 5MP resolution). We used two laser emitters to conduct experiments. The system setup we used for the measurement is shown in Fig. 8.

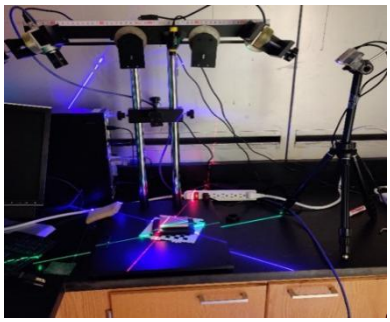

Fig. 8. Proposed structured-light measurement system.

A. System Calibration Results

With the help of MATLAB Camera Calibration toolbox, both extrinsic parameters $[R \quad t]$ and intrinsic matrix A for the cameras are computed based on Zhang's methodology [23]. The calibrated parameters for one camera are shown in (20).

$$A = \begin{bmatrix} 7.742832\times10^{3} & 0 & 0.988623\times10^{3} \\ 0 & 7.759150\times10^{3} & 0.991270\times10^{3} \\ 0 & 0 & 1 \end{bmatrix}$$

$$k_1 = -0.204568, k_2 = 0.808134$$

$$R = \begin{bmatrix} 0.942243 & 0.035153 & 0.333081 \\ -0.033239 & 0.999382 & -0.011445 \\ -0.333278 & -0.000287 & 0.942829 \end{bmatrix} \tag{20}$$

$$t = \begin{bmatrix} 0.0164085\times10^{2} \\ -0.307983\times10^{2} \\ 6.601462\times10^{2} \end{bmatrix}$$

From the checkerboard images generated by the sequential laser emitter projections, two planes obtained as following:

$$\pi_1 = \begin{bmatrix} 6.303903\times10^{-3} \\ 2.015055\times10^{-3} \\ 1.479567\times10^{-3} \end{bmatrix} \quad \pi_2 = \begin{bmatrix} 0.192598\times10^{-3} \\ 0.793808\times10^{-3} \\ 1.561986\times10^{-3} \end{bmatrix} \tag{21}$$

B. Height Measurement and Results

Fig. 9 show the object used for height measurement using our structured light vision system. The object is placed on the operating table during the measurement. We obtain six groups of object images, each group consisting of three pictures. Fig. 9 displays the images labeled from m1 to m6 from two laser emitters.

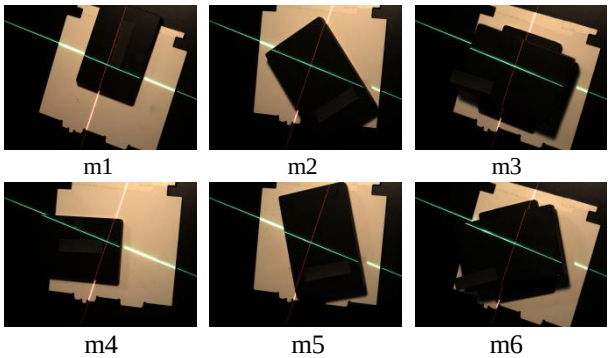

Fig. 9 Measurement for m1 to m6.

The height measurement results two cameras and two laser emitters are listed in Table 1, while Tables 2 includes the worst results from the single camera and two laser emitters. The first column in Tables 1 and 2 are the actual heights via physical measurements; meanwhile, the heights measured with multi-level RANSAC algorithm are presented in the second column of Tables 1 and 2. The MLRANSAC algorithm has 3.65% obtained from averaging the relative errors from the six objects. It clear that the multiple camera and multiple laser emitter system outperforms the system equipped with a single camera

and multiple laser emitters. In Table 3, we compare the obtained results using the multi-level RANSAC algorithm with existing methods, that is, time division and color division [26]. The MLRANSAC algorithm outcompetes for most measurements.

Table 1 Multi-level RANSAC algorithm with two cameras

Measurement Number	Actual height / mm	Measure height / mm	Absolute error / mm	Relative error / %
1	6.700	6.839	0.139	2.08%
2	12.800	12.386	0.414	-3.23%
3	19.500	18.165	1.335	-6.85%
4	6.700	6.942	0.242	3.61%
5	12.800	12.373	0.427	-3.34%
6	19.500	18.488	1.012	-5.19%

Table 2 Multi-level RANSAC algorithm with a single camera

Measurement Number	Actual height / mm	Measure height / mm	Absolute error / mm	Relative error / %
1	6.700	6.787	0.087	1.30%
2	12.800	11.851	0.949	-7.41%
3	19.500	17.524	1.976	-10.13%
4	6.700	7.027	0.327	4.87%
5	12.800	11.849	0.951	-7.43%
6	19.500	17.666	1.834	-9.40%

Table 3 Comparison among time division, color division, and multi-level RANSAC algorithm

Measurement / Relative error	Time division	Color division	MLRANSAC single camera	MLRANSAC two cameras
1	3.01%	6.92%	**1.30%**	**2.08%**
2	**-2.01%**	3.90%	-7.41%	-3.23%
3	-2.92%	**1.20%**	-10.13%	-6.85%
4	4.20%	8.29%	4.87%	**3.61%**
5	-3.82%	6.34%	-7.43%	**-3.34%**
6	-5.96%	3.80%	-9.40%	**-5.19%**

C. 3D Reconstruction Results

Fig. 10 displays 3D reconstructions for one of our tested objects using our proposed method.

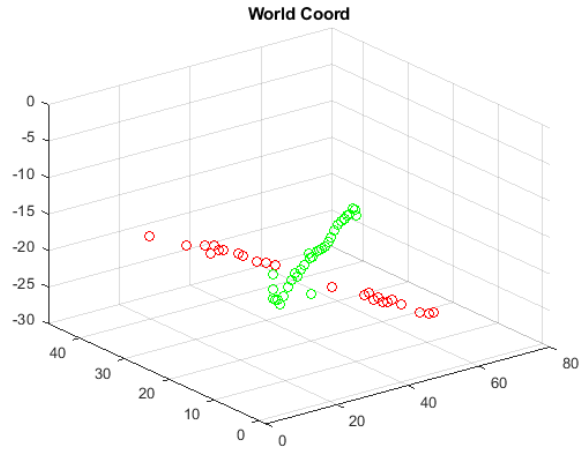

Fig. 10. 3D reconstruction of m6 with the MLRANSAC algorithm.

V. Conclusions

In this paper, we have derived a framework for 3D reconstruction and object height measurement using multiple cameras and multiple laser emitters. We have developed a new multi-level random sample consensus (MLRANSAC) algorithm to tackle the intersection points on the projected image plane due to the multi-laser emitters. Our experiments demonstrate that the system with multiple cameras and multiple laser emitters using the multi-level RANSAC (MLRANSAC) algorithm improves the accuracy of height measurement over the single camera. In future work, we will compare 3D reconstruction error among our method and other approaches; especially, the method with cameras only will be compared later.

References

[1] G. Godin et al., "Laser range imaging in archaeology: issues and results," 2003 Conference on Computer Vision and Pattern Recognition Workshop, 2003.

[2] H. Ha, T.-H. Oh, and I. S. Kweon, "A multi-view structured-light System for highly accurate 3D modeling," 2015 International Conference on 3D Vision, 2015.

[3] C. Ho, "Machine vision based 3D scanning system," in 2009 9th International Conference on Electronic Measurement & Instruments, 2009, pp. 4-445-4-449: IEEE.

[4] J. Li, G. Liu, and Y. Liu, "A dynamic volume measurement system with structured light vision," in 2016 31st Youth Academic Annual Conference of Chinese Association of Automation (YAC), 2016, pp. 251-255: IEEE.

[5] M. Garrido, M. Perez-Ruiz, C. Valero, C. Gliever, B. Hanson, and D. Slaughter, "Active optical sensors for tree stem detection and classification in nurseries," Sensors, vol. 14, no. 6, pp. 10783–10803, 2014.

[6] D. Li, H. Zhang, Z. Song, D. Man, and M. W. Jones, "An automatic laser scanning system for accurate 3d reconstruction of indoor scenes," in 2017 IEEE International Conference on Information and Automation (ICIA), 2017, pp. 826-831: IEEE.

[7] J. Deng, B. Chen, X. Cao, B. Yao, Z. Zhao, and J. Yu, "3D reconstruction of rotating objects based on line structured-light scanning," in 2018 International Conference on Sensing, Diagnostics, Prognostics, and Control (SDPC), 2018, pp. 244-247: IEEE.

[8] Y. Zheng, J. Li and L. Wu, "Tree radial growth measurement system based on line structured light vision," 2019 IEEE International Conference on Power, Intelligent Computing and Systems (ICPICS),2019, pp. 334-337: IEEE.

[9] F. Mokhayeri, E. Granger and G. Bilodeau, "Domain-specific face synthesis for video face recognition from a single sample per person," in IEEE Transactions on Information Forensics and Security, 2019, pp. 757-772: IEEE.

[10] B Ayhan, C Kwan, "Mastcam Image Resolution Enhancement with Application to Disparity Map Generation for Stereo Images with Different Resolutions," Sensors 19 (16), 2019, pp. 3526: MDPI.

[11] C Kwan, B Chou, B Ayhan, "Enhancing Stereo Image Formation and Depth Map Estimation for Mastcam Images," 2018 9th IEEE Ubiquitous Computing, Electronics & Mobile Communication Conference, 2018, pp. 566-572: IEEE.

[12] C Kwan, B Chou, B Ayhan, "Stereo Image and Depth Map Generation for Images with Different Views and Resolutions," 2018 9th IEEE Ubiquitous Computing, Electronics & Mobile Communication Conference, 2018, pp. 573-579: IEEE.

[13] J. Fan, F. Jing, L. Yang, L. Teng, and M. Tan, "A precise initial weld point guiding method of micro-gap weld based on structured light vision sensor," IEEE Sensors Journal, vol. 19, no. 1, 2019, pp. 322-331: IEEE.

[14] S. R. Fanello et al., "HyperDepth: learning depth from structured light without matching," presented at the 2016 IEEE Conference on Computer

Vision and Pattern Recognition (CVPR), 2016.
[15] C. Holenstein, R. Zlot, and M. Bosse, “Watertight surface reconstruction of caves from 3D laser data,” 2011 IEEE/RSJ International Conference on Intelligent Robots and Systems, 2011.
[16] X. Chen et al., “A structured-light-based panoramic depth camera,” 2018 IEEE International Conference on Real-time Computing and Robotics (RCAR), 2018, pp. 102-107: IEEE.
[17] D. Scharstein and R. Szeliski. “High-accuracy stereodepth maps using structured light,” In CVPR, 2003.
[18] M. Vo, S. G. Narasimhan, and Y. Sheikh, “Texture illumination separation for single-shot structured light reconstruction,” IEEE Trans Pattern Anal Mach Intell, vol. 38, no. 2, pp. 390-404, Feb 2016.
[19] H. Ha, T.-H. Oh, and I. S. Kweon, “A multi-view structured-light System for highly accurate 3D modeling,” presented at the 2015 International Conference on 3D Vision, 2015.
[20] Y. Zou and R. Lan, “An end-to-end calibration method for welding robot laser vision systems with deep reinforcement learning,” in IEEE Transactions on Instrumentation and Measurement, 2020, pp. 4270-4280: IEEE.
[21] L. Zhang, J. Lin, J. Sun, G. Yin, C. Ma, and L. Nie, “A robust stripe segmentation method for 3D measurement of structured light,” 2015 IEEE International Conference on Mechatronics and Automation (ICMA), 2015, pp. 2431-2436: IEEE.
[22] Bouguet, J.Y. Camera Calibration Toolbox for Matlab; California Institute of Technology: Pasadena, CA, USA, 2013.
[23] Z. Zhang, “Flexible camera calibration by viewing a plane from unkown orientations,” Proceedings of the Seventh IEEE International Conference on Computer Vision, September 1999.
[24] W. Li, P. Wang, B. Li and B. Li, “Structured-light binocular vision system for dynamic measurement of rail wear,” 2019 IEEE 2nd International Conference on Electronics Technology (ICET), Chengdu, China, 2019, pp. 547-551: IEEE.
[25] C. Wang, Y. Li, Z. Ma, J. Zeng, T. Jin and H. Liu, “Distortion rectifying for dynamically measuring rail profile based on self-calibration of multiline structured light,” in IEEE Transactions on Instrumentation and Measurement, 2018, pp. 678-689: IEEE.
[26] Y. Zhang, Z. Luo, J. Hou, L. Tan and X. Guo, “Computer vision techniques for improving structured light vision systems,” 2020 IEEE International Conference on Electro Information Technology (EIT), 2020.
[27] Z. Feng, D. Man and Z. Song, “A pattern and calibration method for single-pattern structured light system,” in IEEE Transactions on Instrumentation and Measurement, 2020, pp. 3037-3048: IEEE.